Technology in Cancer Research and Treatment
ISSN 1533-0346
Volume 13, Number 6, December 2014

Quantitative Assessment of Cancer Vascular Architecture by Skeletonization of High-resolution 3-D Contrast-enhanced Ultrasound Images: Role of Liposomes and Microbubbles

F. Molinari, Ph.D.[1]*
K. M. Meiburger, Ph.D Student[1]
P. Giustetto, B.Sc.[2,3]
S. Rizzitelli, Ph.D. Student[2]
C. Boffa, Ph.D. Student[2]
M. Castano, Ph.D.[4]
E. Terreno, Ph.D.[2,3]

[1]Biolab, Department of Electronics and Telecommunications, Politecnico di Torino, Torino, Italy
[2]Department of Molecular Biotechnology and Health Sciences, Molecular Imaging Center, University of Torino, Torino, Italy
[3]Center for Preclinical Imaging, University of Torino, Torino, Italy
[4]Bracco Research Center, Bracco Imaging S.p.A., Colleretto Giacosa, Torino, Italy

www.tcrt.org
DOI: 10.7785/tcrtexpress.2013.600272

The accurate characterization and description of the vascular network of a cancer lesion is of paramount importance in clinical practice and cancer research in order to improve diagnostic accuracy or to assess the effectiveness of a treatment. The aim of this study was to show the effectiveness of liposomes as an ultrasound contrast agent to describe the 3-D vascular architecture of a tumor. Eight C57BL/6 mice grafted with syngeneic B16-F10 murine melanoma cells were injected with a bolus of 1,2-Distearoyl-sn-glycero-3-phosphocoline (DSPC)-based non-targeted liposomes and with a bolus of microbubbles. 3-D contrast-enhanced images of the tumor lesions were acquired in three conditions: pre-contrast, after the injection of microbubbles, and after the injection of liposomes. By using a previously developed reconstruction and characterization image processing technique, we obtained the 3-D representation of the vascular architecture in these three conditions. Six descriptive parameters of these networks were also computed: the number of vascular trees (NT), the vascular density (VD), the number of branches, the 2-D curvature measure, the number of vascular flexes of the vessels, and the 3-D curvature. Results showed that all the vascular descriptors obtained by liposome-based images were statistically equal to those obtained by using microbubbles, except the VD which was found to be lower for liposome images. All the six descriptors computed in pre-contrast conditions had values that were statistically lower than those computed in presence of contrast, both for liposomes and microbubbles. Liposomes have already been used in cancer therapy for the selective ultrasound-mediated delivery of drugs. This work demonstrated their effectiveness also as vascular diagnostic contrast agents, therefore proving that liposomes can be used as efficient "theranostic" (*i.e.* therapeutic + diagnostic) ultrasound probes.

Key words: Contrast-enhanced ultrasounds; Molecular imaging; Skeletonization; Distance transform; Microbubbles; Liposomes; Vascular descriptors; Vascular architecture.

Introduction

Sonography is a non-invasive imaging modality allowing the real-time visualization of cancer lesions in almost any organ of the human body, except lungs and the gastric tract (where the presence of air could limit the propagation of the ultrasound waves). Due to their excellent penetration capabilities, sonography has been used to visualize thyroid (1, 2), pancreas (3), liver (4), prostate (5), ovarian

Abbreviations: HRUS: High-resolution Ultrasound; CEUS: Contrast-enhanced UltraSound; DT: Distance Transform; NT: Number of Vascular Trees; VD: Vascular Density; NB: Number of Branching Nodes; DM: 2-D Distance Metric; ICM: Inflection Count Metric; SOAM: 3-D Sum of Angles Metric.

*Corresponding author:
F. Molinari, Ph.D.
Phone: +39 11 564 4135
E-mail: filippo.molinari@polito.it

(6, 7), breast (8), and brain (9) cancers. When used in traditional B-mode modality, sonographic devices show a gray image in which the pixel intensity (brightness) is proportional to the logarithmic amplitude of the ultrasound echo generated in that portion of tissue. In cancer diagnosis, B-mode imaging allows detection of the presence of a lesion. A sample image of a mouse syngeneic cancer model (C57BL/6 mouse with subcutaneous grafting of B16-F10 murine syngeneic melanoma cancer cells) is shown in Figure 1A. When used in Doppler modality, sonographic devices also allow the observation of blood flow velocity, since the gray B-Mode image is overlaid by a color map showing either the direction and the value of the blood flow (Color Doppler mode) or just the value of the blood flow (Power Doppler mode). Color and Power Doppler images are, however, limited in resolution and cannot detect blood flows in microvasculature (10) (Figure 1B).

Previous works have shown that the characterization of cancer lesion vascular patterns are not possible with Doppler imaging alone, because of the lack of spatial resolution (11, 12). Contrast-enhanced ultrasound (CEUS) imaging can be used to effectively assess the vascularization of tumors *in vivo* (13, 14). CEUS imaging relies on second harmonic non-linear imaging (Figure 1C). In this image, the signal is spontaneously generated by the non-linear behavior of both tissues and blood (15). However, second harmonic imaging mainly exploits the non-linear properties of the contrast agent, consisting of gas-filled microbubbles. Such microbubbles have an average diameter of about 5 μm and do not extravasate, but they have limited duration in the blood flow (16). A sample of CEUS imaging is shown in Figure 1D.

3-D CEUS imaging allows an accurate reconstruction of cancer vascular patterns (17, 18). Huang *et al.* showed that it is possible to reconstruct the spatial vascular pattern of breast cancer lesions by using 3-D ultrasound imaging (19, 20). Their approach consisted of two steps: first the Power Doppler images were segmented in order to detect only the voxels

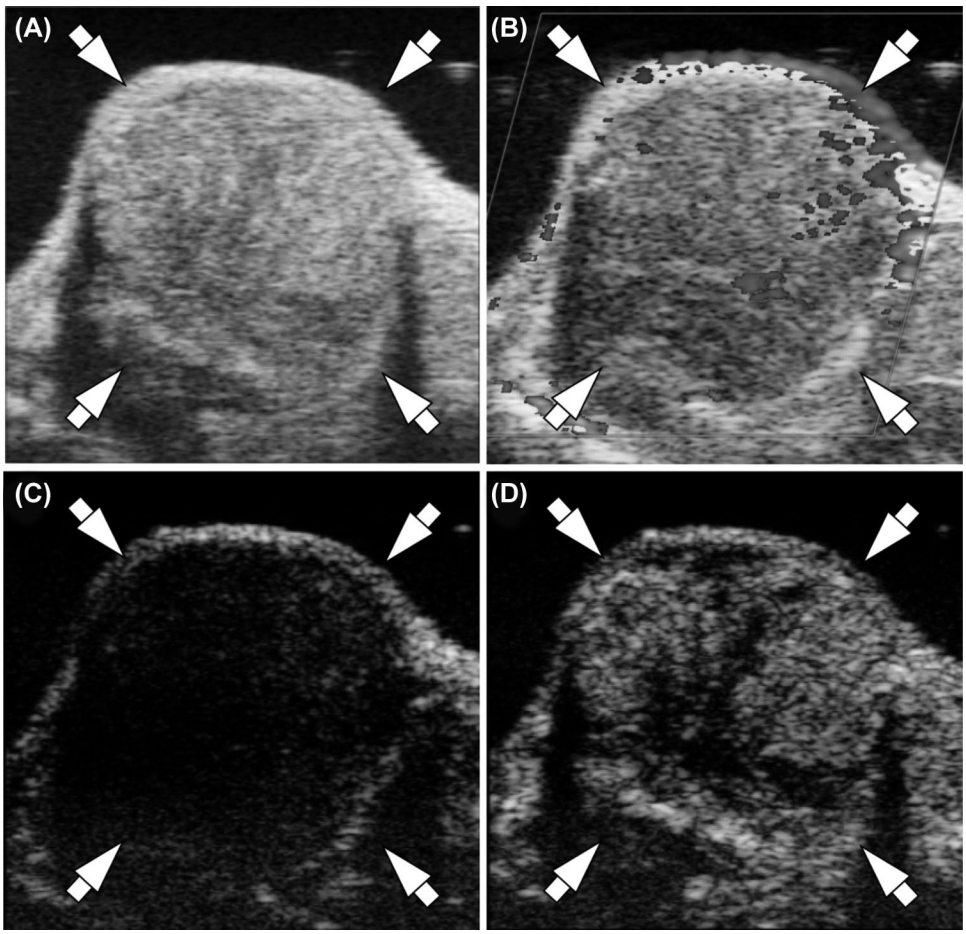

Figure 1: Ultrasound images of a mouse tumor (C57BL/6 mouse with subcutaneous grafting of syngeneic melanoma induced by B16-F10 cancer cells). (**A**) High-resolution B-mode, (**B**) Power Doppler, (**C**) Second harmonic non-linear spontaneous signal, and (**D**) CEUS image after injection of microbubbles. The white arrows indicate the cancer lesion borders.

in which blood flow was present, and then the set of voxels was post-processed by thinning algorithms in order to reconstruct the internal vascular architecture. In 2010, Molinari *et al.* proposed a quantitative approach for the characterization of thyroid nodules that was based on 3-D CEUS imaging (18). The 3-D representation of the tumor vascularization can also be characterized by computing numerical features of the vascular pattern, such as the number of vascular trees (NT), the number of vascular branches, and the tortuosity of the vessels (18). Acharya *et al.* then showed that such numerical CEUS features could be used for the differential diagnosis of malignant lesions w.r.t. benign ones (1, 21).

Liposomes, which are nano-sized vesicles, are widely used in medicine as drug carriers, mostly in cancer therapy (22, 23). Recently, researchers have been facing the challenge of developing innovative strategies to provide an imaging support to therapies, including the design of probes for the *in vivo* visualization of drug delivery and release (24, 25). This field is called "theranosis", which comes from merging the words "therapy" and "diagnosis", and it indicates the use of the same agent for diagnosis and therapy (26). Liposomes play a relevant role in this emerging research field, mainly thanks to the fact that they are very versatile and can therefore be loaded with drugs and diagnostic agents that present different physico-chemical characteristics. Therefore, liposomes present the characteristics of a probe that can potentially be used to both characterize and treat a cancerous lesion.

The aim of this study was to quantitatively compare tumor vascular patterns as assessed by 3D CEUS when using traditional microbubbles and liposomes. The study was conducted on animal models using dedicated ultrasound equipment, however the processing technique used is general and easily adaptable to human studies.

Methods

Liposomes Preparation

DSPC[1] liposomes were prepared using the thin film hydration method. The total amount of lipidic material was 50 mg/mL. The liposomes were formulated as follows: DSPC/ DSPE-PEG2000[2] (95/5 molar ratio). Chemicals were purchased from Avanti Polar Inc. (Alabaster, AL, USA). The thin lipid film was hydrated with a 300 mM solution of the clinically approved MRI agent Gadoteridol (marketed by Bracco Imaging as ProHance™) and the so-obtained suspension was extruded several times on polycarbonate filters. The mean hydrodynamic liposomes diameter was 160 ± 10 nm (determined by dynamic light scattering) and the final concentration of Gadoteridol in the liposomes suspension was 30 mM. We used liposomes with an internal core of an MRI contrast agent because in another related study we showed that these liposomes were visible by ultrasound imaging and that their release could be controlled by non-focused ultrasounds (22).

Experimental Protocol

We tested eight C57BL/6 male mice (10 weeks old, weight 23 ± 4 g) purchased from Charles River Laboratories (Calco, Lecco, Italy). B16-F10 murine melanoma cells, cultured in RPMI 1640 medium supplemented with 10% (v/v) heat-inactivated fetal calf serum, 100 UI/mL penicillin, and 100 mg/mL streptomycin, were inoculated 1×10^6 in 0.2 mL PBS subcutaneously to obtain a syngeneic melanoma in the rear thigh of the mice. All the experiments were performed around 1 week after the injection, when the tumor's maximum diameter reached about 8 mm.

The mice were sedated by gaseous anaesthesia according to the protocols for preclinical studies (27). Ultrasound examinations were performed with a VEVO2100 system (Fujifilm VisualSonics, Toronto, Canada) equipped with a 24 MHz linear probe. Traditional high-resolution ultrasound (HRUS) images were acquired, along with 3-D CEUS images of the tumor. First we acquired a basal 3-D HRUS and CEUS image of the lesion (without any contrast). Then we injected a 50 μL bolus of non-targeted Vevo MicroMarker (Bracco, Geneve) optimized for use on the Visualsonics HR Micro-Ultrasound System VEVO2100. 40 μL of saline solution was injected right after the contrast agent bolus. We then acquired the 3-D HRUS and CEUS images. After waiting for the complete destruction of the microbubbles (about 30 minutes), a 200 μL bolus of the above described liposomes was then injected, followed by 40 μL of saline solution. After the liposomes injection, we again acquired the 3-D HRUS and CEUS images. The Gain and Time Gain Compensation (TGC) settings of the ultrasound system were kept the same for all exams.

Experiments were performed according to the national regulations and were approved by the local animal experiments ethical committee.

Pre-processing and Skeletonization Strategy

The pre-processing strategy of the images was the same for the three different 3-D CEUS volumes. The pre-processing steps are fully described in a previous work (18), and is summarized here in Figure 2. The first column of Figure 2 reports the processing steps applied to the pre-contrast CEUS image

[1] 1,2-Distearoyl-sn-glycero-3-phosphocoline (DSPC)
[2] 1,2 Distearoyl-sn-glycero-3-phosphoethanolamine-N-[methoxy(polyethyleneglycol)-2000]Ammonium salt (DSPE-PEG2000)

(*i.e.* before the injection of any contrast), the middle column is relative to the CEUS image acquired after the injection of microbubbles, and the rightmost column is relative to the injection of liposomes. Only the central slice of the 3-D volumes is represented. The cancer lesion and the slice are the same in all three columns. The rows of Figure 2 report the sequence of the pre-processing steps. The first row shows the raw CEUS image; the second row portrays the image after intensity normalization; and the third row image after low-pass filtering (Gaussian filtering with a 3×3 kernel and $\sigma = 1$). After filtering, the images were morphologically opened in order to emphasize the intensity signal given by the contrast agent (fourth row of Figure 2). We used a structuring element of 1 pixel radius, because it resembled the shape of a bubble.

Each slice was then segmented by using Otsu's thresholding (28). The bottom row of Figure 2 reports the segmentation mask, in which the white region indicates the presence of contrast agent.

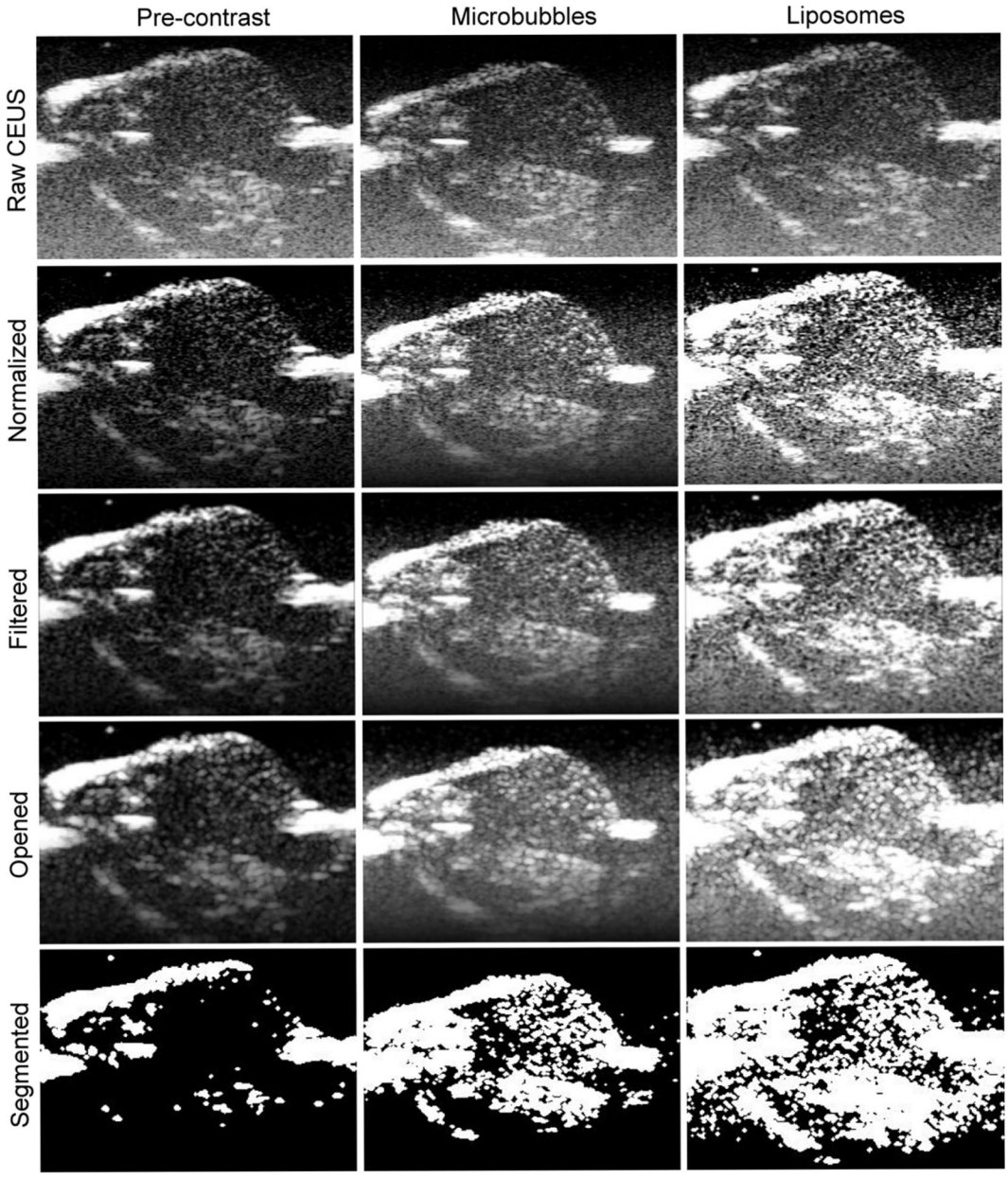

Figure 2: Pre-processing architecture. The first column is relative to a central slice of the tumor before injection of any contrast, the second to the injection of microbubbles, and the third to the injection of liposomes. The rows report the pre-processing steps (from top to bottom): the raw image, the intensity normalized image, the filtered image, the morphologically opened image, and the result of the segmentation based on Otsu's thresholding.

Once the slices were processed and segmented, we applied a skeletonization process to reduce the representation of the vascular network. The skeletonization procedure aims at reducing the image into a minimal representation that still preserves morphology (29). This skeleton-based approach has already been used in previous ultrasound studies (12, 18), in which there was the need to reduce the representation of the blood vessels without losing the architectural features of the vascular pattern. Our skeletonization procedure consisted in two cascaded steps:

1 We first adopted a geometrical skeleton based on the distance transform (DT) (30). The DT of a point belonging to an object is defined as its minimal distance from the closest border of the object itself. Hence, points located in the middle of a vessel have high DT values, whereas points located near the vessel borders have lower DT values. Therefore, a DT skeleton can be obtained by simply imposing a threshold on the DT of an image, thus preserving the innermost points of the objects. The higher the threshold, the thinner the object representation will be. In previous works, we showed that a suitable value for CEUS DT skeletons is 0.55 (18). Figure 3 sketches the skeletonization process. In particular, Figure 3B shows the DT skeleton obtained by the segmented CEUS image of Figure 3A.

2 The DT skeleton was then thinned even more with the use of a topological skeleton. We used the skeleton proposed by Ma and Sonka (29). Topological skeletons are based on a series of $3 \times 3 \times 3$ masks. These masks describe all the possible conditions to consider a pixel as a "border" pixel. Hence, if the $3 \times 3 \times 3$ neighborhood of a pixel matches one of the masks, that pixel is located on the border of an object and can thus be deleted. Full details about the Ma and Sonka algorithm (29) can also be found in the study by Palàgyi and Kuba (31), in which 38 masks were used. Figure 3C reports the topological skeleton obtained from the DT skeleton of Figure 3B. Figure 3D shows the final skeleton in red overlaid on top of the original CEUS image.

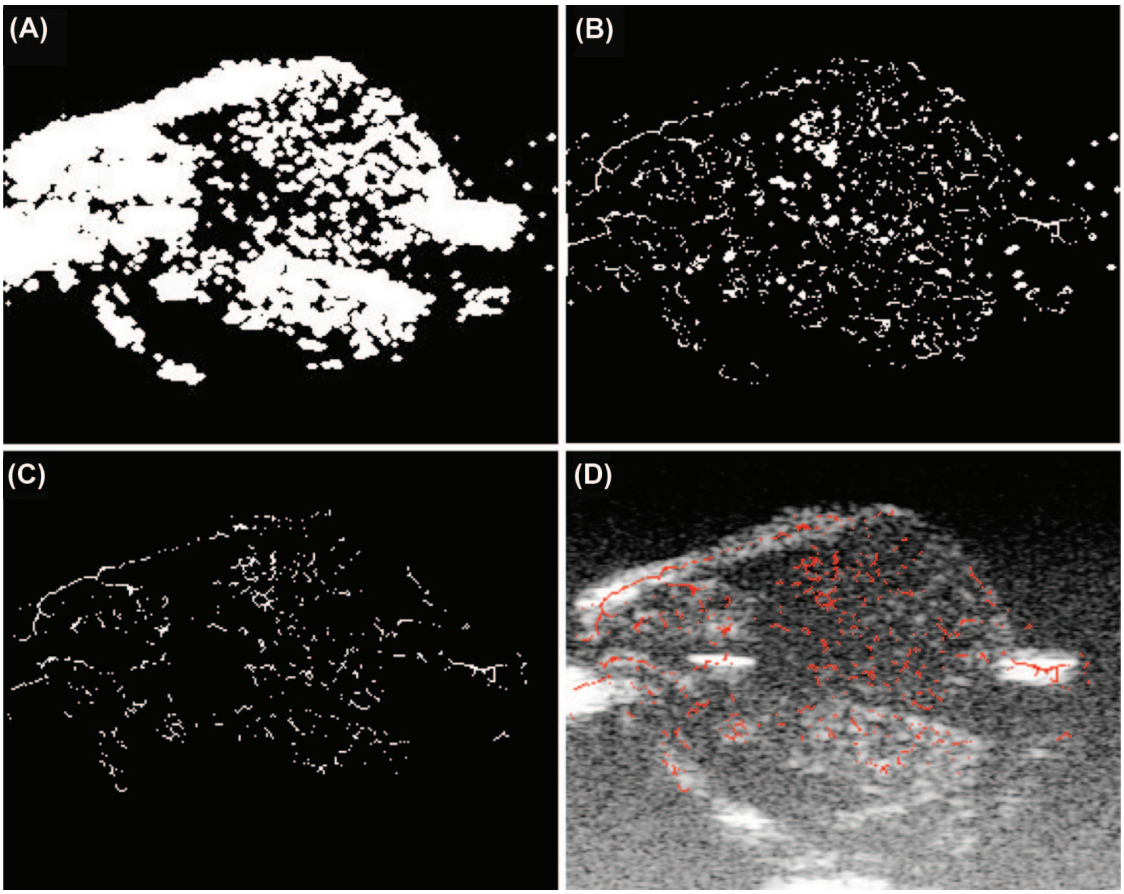

Figure 3: Skeletonization process. This sample is relative to the injection of microbubbles. (**A**) Pre-processed image (same as Figure 2, middle column, bottom row), (**B**) Application of the Distance Transform geometric skeleton, (**C**) Application of the topological skeleton, and (**D**) Final skeleton (in red) overlaid on the original CEUS image.

Vascular Pattern Characterization

Basically, the obtained 3-D skeletons are volumetric binary images containing a network of vessels. Therefore, such networks can be analyzed in order to numerically describe the represented vascular pattern. Each 3-D skeleton was hence analyzed by the Breadth First Search (BFS) algorithm (32). Since cancer lesions can have different sizes, we analyzed a Region-of-Interest (ROI) of $50 \times 50 \times 20$ pixels, in order to standardize the quantification of the vascular pattern. We chose this size because it was compatible with the dimensions of all the cancer lesions of our dataset. Figure 4 shows the positioning of the ROI with respect to the 3-D skeleton. The positioning of the ROI was made manually.

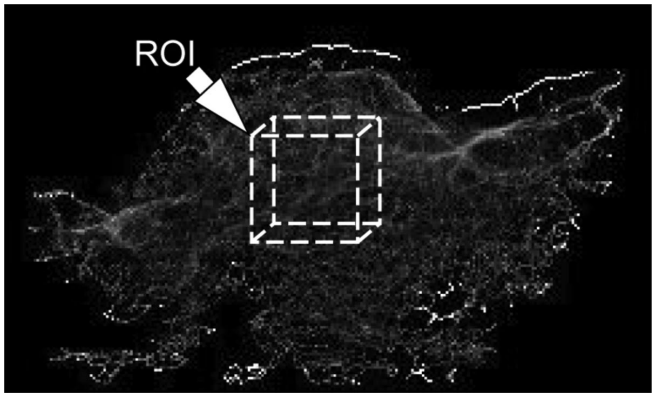

Figure 4: Manual positioning of the Region-of-Interest (ROI) in the center of the 3-D skeleton. The ROI size was $50 \times 50 \times 20$ pixels.

Starting from an initial voxel, the BFS algorithm navigates the entire skeleton by following the vessels. The BFS marks each voxel as visited and iterates until all voxels of the skeleton have been visited at least once. The BFS algorithm is able to search all of the vessels in the skeleton and during this search, quantitative parameters can be computed. The six parameters that we considered indicative of the vascular pattern were:

1 Number of vascular trees (NT): Defined as the number of trees in which the BFS decomposes the skeleton image.
2 Vascular density (VD): Defined as the number of skeleton voxels compared to the volume of the selected ROI.
3 Number of branching nodes (NB): Defined as the number of branches of the structure.
4 2-D distance metric (DM): A measure of the bidimensional tortuosity of a vessel. Considering a curved line representing the vessel, the DM is defined as the ratio between the actual length of the curve and the Euclidean distance between the first and last point of the curve. The DM value of a straight line would be equal to 1, but it would assume higher values as the curvature increases.
5 Inflection count metric (ICM): Defined as the number of flexes of a curve. This is another measurement of vessel tortuosity.
6 3-D sum of angles metric (SOAM): Defined as the sum of all the angles that a curve has in space.

The mathematical description of these parameters can be found in previously published papers (18, 19). By summarizing, we characterized the vascular complexity by three morphological parameters (NT, VD, and NB) and by three curvature/tortuosity parameters (DM, ICM, and SOAM).

Results

The advantages of the proposed two-step skeletonization architecture are:

1 Prevention of vessel disconnections, because the DT skeleton cannot create disconnections unless a wrong (*i.e.* too high) threshold is selected;
2 Reduction of the computational cost, because the computationally expensive topological skeleton is applied to an already reduced set of voxels.

Figure 5 reports the obtained skeletons from the three sets of CEUS images for a cancer lesion of our dataset. The first column of Figure 5 is relative to the tumor before injection of any contrast, the second to the injection of microbubbles, and the third to the injection of liposomes. The first row Figure 5 portrays the original CEUS images (central slice of the tumor); the second row reports the corresponding skeletonized images; the bottom row instead shows the 3-D reconstructed skeletons. It is possible to observe that the 3-D skeletons obtained after injections of microbubbles or liposomes are very rich and represent the intra-lesion vasculature very nicely. Conversely, the skeleton obtained from the raw CEUS images without any contrast is limited to the periphery of the lesion, and there is no representation of the internal vessels.

Table I reports the average values of the vascular descriptors. The values were measured on the 3-D CEUS volumes after skeletonization.

The first comparison is between the vascular descriptors obtained by using liposomes and microbubbles (second and third rows). The asterisks in Table I denote the descriptors that were not statistically different between the 3-D microbubbles and 3-D liposomes CEUS skeletons (paired Student's *t*-test; $p > 0.05$). Five out of six descriptors were

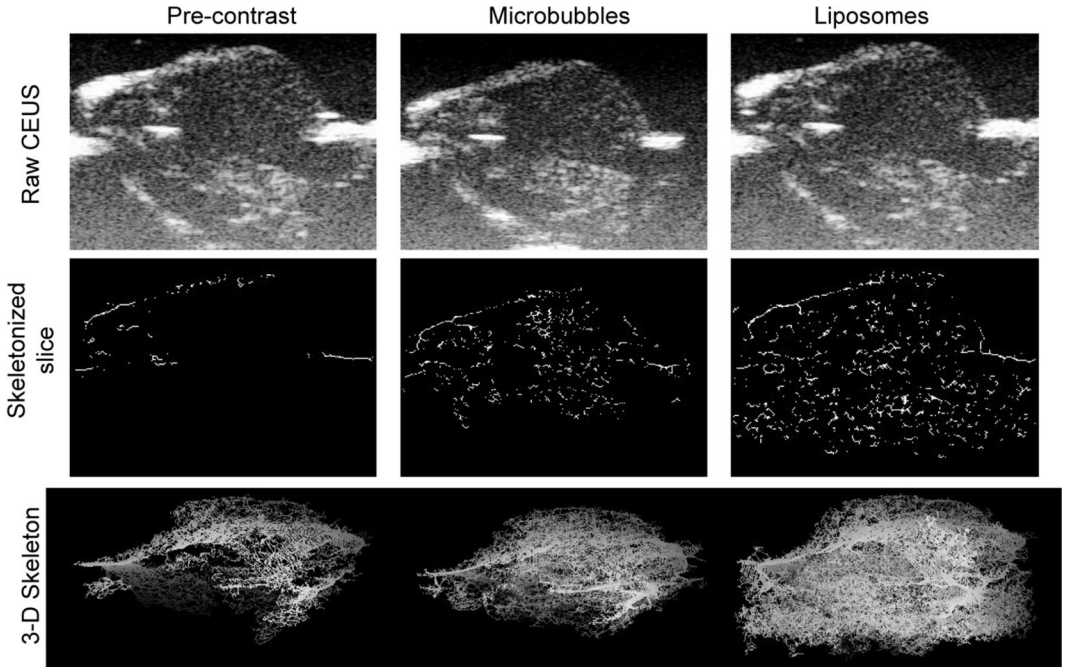

Figure 5: Representation of the final 3-D skeletons. The first column is relative to the tumor before injection of any contrast, the second to the injection of microbubbles, and the third of liposomes. The first row reports the original CEUS image (central slice of the tumor); the second row reports the corresponding skeletonized image; the bottom row reports the 3-D reconstructed skeleton.

Table I
Average values of the six descriptors of the vascular patterns as measured from the 3-D CEUS skeletons.

	NT*	VD	NB*	DM*	ICM*	SOAM*
Pre-contrast	14.3 ± 6.2	0.01 ± 0.01	188 ± 146	8.39 ± 4.26	3.76 ± 2.73	4.49 ± 3.08
Microbubbles	39.5 ± 17.5	0.07 ± 0.01	1096 ± 357	23.70 ± 3.57	7.86 ± 3.57	12.17 ± 6.41
Liposomes	38.1 ± 17.2	0.05 ± 0.03	695 ± 450	23.11 ± 12.08	9.88 ± 5.45	11.08 ± 6.00

*The descriptors that were not statistically different between microbubbles and liposomes (paired Student's *t*-test; $p > 0.05$).

Abbreviations: NT: Number of Vascular Trees; VD: Vascular Density; NB: Number of Branching nodes; DM: 2-D Distance Metric; ICM: Inflection Count Metric; SOAM: 3-D Sum of Angles Metric.

not statistically different, whereas one (VD) was higher for microbubbles than for liposomes ($p = 0.01$). The average NT detected in the ROIs from 3-D CEUS skeletons obtained after the injection of microbubbles was equal to 39.5 ± 17.5 (38.1 ± 17.2 after liposomes injection), whereas the average NB was 1096 ± 357 (695 ± 450 after liposomes injection). The three curvature/tortuosity descriptors were equal to 23.70 ± 3.57 (DM), 7.86 ± 3.57 (ICM), and 12.17 ± 6.41 (SOAM) for microbubbles-based skeletons. For liposomes-based skeletons the three descriptors had the following respective values: 23.11 ± 12.08 (DM), 9.88 ± 5.45 (ICM), and 11.08 ± 6.00 (SOAM). It is, therefore, possible to notice that the values reported by both the second and third rows are very close, thus demonstrating the effectiveness of liposomes as a potential alternative to microbubbles for the quantification and characterization of cancer vascularization with 3-D ultrasound images.

The second comparison is among the vascular descriptors measured by the pre-contrast skeletons and the respective descriptors measured after microbubbles or liposomes injection. The values of the six descriptors measured in pre-contrast conditions were: 14.3 ± 6.2 (NT), 0.01 ± 0.01 (VD), 188 ± 146 (NB), 8.39 ± 4.26 (DM), 3.76 ± 2.73 (ICM), 4.49 ± 3.08 (SOAM). All the descriptor values were statistically lower in the pre-contrast condition than in the contrast condition (paired Student's *t*-test; always $p < 0.05$), independently on the type of contrast (*i.e.* microbubbles or liposomes).

Discussion

The reconstruction and numerical characterization of a tumor lesion vasculature could be very useful in practical applications, in basic research, and in pharmacological and oncological applications. Previous studies have demonstrated that the characterization of the internal vascularization of breast lesions could be useful in clinical practice to aid the differential diagnosis between benign and malignant lesions. Huang *et al.* showed that the descriptors of the vascular architecture of a lesion could be used to assess malignancy in breast lesions (19). They used 3-D volumes obtained by Power Doppler imaging, therefore their data were mainly relative to macro-vessels. They showed that malignant lesions had higher values of the vascular descriptors. This is due to the fact that tumor angiogenesis creates new vessels with a high number of branches, and that the neo-formed vessels are usually coiled. More recently, the same team showed that malignant lesions can be efficiently detected by comparing the vascular descriptors of the suspected lesion with the descriptors measured on a portion of healthy tissue taken as reference (20). Molinari *et al.* applied a similar technique to show the difference between the intranodal vascularization of benign and malignant thyroid lesions (18), and they demonstrated that the numerical values of the vascular descriptors measured by the skeletons are higher for malignant lesions than for benign lesions. Molinari *et al.* used CEUS imaging (18), thus showing the effectiveness of this approach to describe the micro-vascularization of a tumor. Therefore, this combined approach of 3-D reconstruction and description of the vascular architecture finds its application in the field of cancer research and treatment.

In this work, conducted on animal models, we showed that the injection of a bolus of liposomes produces CEUS 3-D volumes that are suitable for the reconstruction and characterization of the microvascularization of a lesion. We demonstrated that the 3-D skeletons depicting the intra-lesion vascular network obtained after liposomes injection are very similar to those obtained after injecting the traditional sonographic contrast agent consisting of gaseous microbubbles. We reconstructed the skeleton of the vascular network of eight mice by injecting microbubbles and liposomes separately, and then showed that the numerical values of the vascular descriptors were on average not statistically different. Specifically, we showed that the NT, the number of branches, and the curvature and tortuosity indexes were not statistically different when measured after microbubbles or liposomes injection (Table I).

We found that one out of six parameters (VD) was statistically lower for liposome-based skeletons than for microbubbles skeletons. This result was most likely due to the type of liposomes that were used. The DSPC liposomes used in this work likely generated a non-optimal ultrasound signal. Numerically, the average VD measured from 3-D liposome-based CEUS images was not very different from that measured from microbubbles-based images, but the standard deviation was three times higher (Table I). Additionally, the ultrasound equipment used was specifically optimized for the Vevo MicroMarker microbubbles and produced images with higher echogenicity. Hence, it is likely that a suboptimal sonographic response of our liposomes, which produced images with lower echogenicity, gave forth a lower VD average value.

An improved echogenicity of the liposomes could be obtained by changing the liposomal formulation in terms of membrane and core composition. Alternatively, echogenic liposomes (ELIP), *i.e.* liposomes loaded with a mixture of gas and water, could also be tested; however, these liposomes have a more difficult preparation process and often tend to present a large variability in their size (33). The latter issue may significantly limit the performance of the probe due to the fact that large nanoparticles (diameter > 200 nm) reduce the vascular extravasation (34), thereby decreasing considerably their usefulness in cancer therapy. Furthermore, ELIP are not approved for clinical use yet, contrarily to conventional liposomes.

Nevertheless, to the best of our knowledge, this study is the first one demonstrating that it is possible to accurately reconstruct and describe the vascular architecture of a cancer lesion by using liposomes and 3-D non-linear ultrasound imaging. Some very recent studies adopted a CEUS based methodology to improve the assessment of cancer lesions. Specifically, Grouls *et al.* used non-targeted microbubbles and clinically translatable PEGylated targeted microbubbles for the vascular endothelial growth factor receptor type 2 (35). They quantified the microbubbles kinetics in the lesion and showed that targeted microbubbles enabled the distinction between early stages of liver dysplasia and a normal liver. In our study, we used stealth non-targeted liposomes. Therefore, we believe that our technique could have further scopes of improvement if echogenic and targeted liposomes were used.

Our technique has some limitations that we will discuss here in the following. From a technical point of view, the procedure is not fully automated yet. The pre-processing and skeletonization steps are automated and user-independent, but manual placing of the analysis ROI (Figure 4) is required. Different placements of the ROI could lead to different vascular parameters. In pilot experiments (not reported in this paper) we observed a very low intra-operator variability (lower than 0.1% for all the six parameters). Our team has already developed a fully automated version of this procedure that will remove this limitation. The new procedure will incorporate an automated segmentation of the tumor in the 3-D HRUS images. The segmentation mask will be applied

to the 3-D CEUS volume, in order to automatically determine the entire lesion volume. Another limitation of this study is given by the kinetics of the liposomes in the tumor environment (36). Since liposomes might extravasate, their nonlinear signal could become inaccurate in certain conditions. In fact, smaller nanoparticles have a higher therapeutic effect, but they generate a lower ultrasound signal. Liposomes with an average size of 200 nm might be the best compromise. We are currently studying the liposomes kinetics in tumor environment by using ultrasounds, in order to further optimize the CEUS acquisition modality.

Conclusions

In this paper, we showed that liposome-based 3-D CEUS images are suitable to accurately reconstruct and numerically describe the vascular network of tumor lesions. Our integrated technique was based on image processing, skeletonization, and characterization and can describe morphological and geometrical aspects of the vessel network. Even though this study was conducted in a pre-clinical environment, we believe that this approach could be easily translated to human applications in the near future. Our theranostic technique could be useful for the characterization of tumor types, for the differential diagnosis of suspected lesions, and for the assessment of the effect of anti-cancer drugs (*i.e.* anti-angiogenetic drugs).

Conflict of Interest

Mauro Castano is researcher at the Bracco Research Center, Bracco Imaging S.p.A.

The Authors declare the absence of any other conflict of interest related to the reported study. All the material herein reported is original and not published elsewhere.

References

1. Acharya UR, Faust O, Sree SV, Molinari F, Garberoglio R & Suri JS. Cost-effective and non-invasive automated benign and malignant thyroid lesion classification in 3D contrast-enhanced ultrasound using combination of wavelets and textures: a class of ThyroScan algorithms. *Technol Cancer Res Treat 10*, 371-380 (2011). PMID: 21728394
2. Acharya UR, Faust O, Sree SV, Molinari F & Suri JS. ThyroScreen system: high resolution ultrasound thyroid image characterization into benign and malignant classes using novel combination of texture and discrete wavelet transform. *Comput Methods Programs Biomed 107*, 233-241 (2012). DOI: 10.1016/j.cmpb.2011.10.001
3. Faccioli N, Crippa S, Bassi C & D'Onofrio M. Contrast-enhanced ultrasonography of the pancreas. *Pancreatology 9*, 560-566 (2009). DOI: 10.1159/000225960
4. Herbold T, Wahba R, Bangard C, Demir M, Drebber U & Stippel DL. The laparoscopic approach for radiofrequency ablation of hepatocellular carcinoma-indication, technique and results. *Langenbeck's Archives of Surgery/Deutsche Gesellschaft fur Chirurgie 398*, 47-53 (2013). DOI: 10.1007/s00423-012-1018-5
5. Wolff JM & Mason M. Drivers for change in the management of prostate cancer – guidelines and new treatment techniques. *BJU International 109*(Suppl. 6), 33-41 (2012). DOI: 10.1111/j.1464-410X.2012.11218.x
6. Acharya UR, Sree SV, Krishnan MM, Saba L, Molinari F, Guerriero S & Suri JS. Ovarian tumor characterization using 3D ultrasound. *Technology in Cancer Research & Treatment 11*, 543-552 (2012). PMID: 22775335
7. Acharya UR, Sree SV, Saba L, Molinari F, Guerriero S & Suri JS. Ovarian tumor characterization and classification using ultrasound-a new online paradigm. *Journal of Digital Imaging: The Official Journal of the Society for Computer Applications in Radiology 26*(3), 544-553 (2013). DOI: 10.1007/s10278-012-9553-8
8. Boehler T, Zoehrer F, Harz M & Hahn HK. Breast image registration and deformation modeling. *Critical Reviews in Biomedical Engineering 40*, 235-258 (2012). PMID: 22694202
9. Roelcke U. Imaging brain tumors with PET, SPECT, and ultrasonography. *Handbook of Clinical Neurology 104*, 135-142 (2012). DOI: 10.1016/B978-0-444-52138-5.00010-4
10. Uller W, Jung EM, Hornung M, Ross C, Jung W, Schlitt HJ, Stroszczynski C & Agha A. Evaluation of the microvascularization of pathologic parathyroid glands in patients with primary hyperparathyroidism using conventional ultrasound and contrast-enhanced ultrasound. *Clinical Hemorheology and Microcirculation 48*, 95-103 (2011). DOI: 10.3233/CH-2011-1402
11. Varras M. Benefits and limitations of ultrasonographic evaluation of uterine adnexal lesions in early detection of ovarian cancer. *Clinical and Experimental Obstetrics & Gynecology 31*, 85-98 (2004). PMID: 15266758
12. Hoang JK, Lee WK, Lee M, Johnson D & Farrell S. US Features of thyroid malignancy: pearls and pitfalls. *Radiographics 27*, 847-860; Discussion 861-845 (2007). DOI: 10.1148/rg.273065038
13. Gorce JM, Arditi M & Schneider M. Influence of bubble size distribution on the echogenicity of ultrasound contrast agents: a study of SonoVue. *Invest Radiol 35*, 661-671 (2000). PMID: 11110302
14. Bzyl J, Lederle W, Rix A, Grouls C, Tardy I, Pochon S, Siepmann M, Penzkofer T, Schneider M, Kiessling F & Palmowski M. Molecular and functional ultrasound imaging in differently aggressive breast cancer xenografts using two novel ultrasound contrast agents (BR55 and BR38). *European Radiology 21*, 1988-1995 (2011). DOI: 10.1007/s00330-011-2138-y
15. Carerj S, Trono A, Zito C, Ficarra E, Luzza F, Oreto G & Arrigo F. The second tissue harmonic signal: from physics principles to clinical application. *Italian Heart Journal. Supplement: Official Journal of the Italian Federation of Cardiology 2*, 1078-1086 (2001). PMID: 11723610
16. Schneider M. Characteristics of SonoVuetrade mark. *Echocardiography 16*, 743-746 (1999). PMID: 11175217
17. Carraro R, Molinari F, Deandrea M, Garberoglio R & Suri JS. Characterization of thyroid nodules by 3-D contrast-enhanced ultrasound imaging. *Conf Proc IEEE Eng Med Biol Soc 2008*, 2229-2232 (2008). DOI: 10.1109/IEMBS.2008.4649639
18. Molinari F, Mantovani A, Deandrea M, Limone P, Garberoglio R & Suri JS. Characterization of single thyroid nodules by contrast-enhanced 3-D ultrasound. *Ultrasound in Medicine & Biology 36*, 1616-1625 (2010). DOI: 10.1016/j.ultrasmedbio.2010.07.011
19. Huang SF, Chang RF, Moon WK, Lee YH, Chen DR & Suri JS. Analysis of tumor vascularity using three-dimensional power doppler ultrasound images. *IEEE Trans Med Imaging 27*, 320-330 (2008). DOI: 10.1109/TMI.2007.904665
20. Huang YH, Chen JH, Chang YC, Huang CS, Moon WK, Kuo WJ, Lai KJ & Chang RF. Diagnosis of solid breast tumors using vessel analysis in three-dimensional power doppler ultrasound images. *Journal of Digital Imaging: The Official Journal of The Society For Computer Applications in Radiology 26*, 731-739 (2013). DOI: 10.1007/s10278-012-9556-5

21. Acharya UR, Sree SV, Swapna G, Gupta S, Molinari F, Garberoglio R, Witkowska A & Suri JS. Effect of complex wavelet transform filter on thyroid tumor classification in three-dimensional ultrasound. *Proceedings of the Institution of Mechanical Engineers. Part H, Journal of Engineering in Medicine 227*, 284-292 (2013). DOI: 10.1177/0954411912472422
22. Giustetto P, Castelli DD, Boffa C, Rizzitelli S, Durando D, Cutrin JC, Aime S & Terreno E. Release of a paramagnetic magnetic resonance imaging agent from liposomes triggered by low intensity non-focused ultrasound. *Journal of Medical Imaging and Health Informatics 3*, 356-366 (2013). DOI: 10.1166/jmihi.2013.1183
23. Wang J, Sui M & Fan W. Nanoparticles for tumor targeted therapies and their pharmacokinetics. *Current Drug Metabolism 11*, 129-141 (2010). DOI: 10.2174/138920010791110827
24. Ahmed N, Fessi H & Elaissari A. Theranostic applications of nanoparticles in cancer. *Drug Discovery Today 17*, 928-934 (2012). DOI: 10.1016/j.drudis.2012.03.010
25. Terreno E, Uggeri F & Aime S. Image guided therapy: the advent of theranostic agents. *J Control Release 161*, 328-337 (2012). DOI: 10.1016/j.jconrel.2012.05.028
26. Prabhu P & Patravale V. The upcoming field of theranostic nanomedicine: an overview. *Journal of Biomedical Nanotechnology 8*, 859-882 (2012). PMID: 23029995
27. Gargiulo S, Greco A, Gramanzini M, Esposito S, Affuso A, Brunetti A & Vesce G. Mice anesthesia, analgesia, and care, Part II: anesthetic considerations in preclinical imaging studies. *ILAR Journal/National Research Council, Institute of Laboratory Animal Resources 53*, E70-81 (2012). DOI: 10.1093/ilar.53.1.70
28. Otsu N. A Threshold selection method from gray-level histograms. *Systems, Man and Cybernetics, IEEE Transactions on 9*, 62-66 (1979). DOI: 10.1109/TSMC.1979.4310076
29. Ma MC & Sonka M. A fully parallel 3D thinning algorithm and its applications. *Computer Vision and Image Understanding 64*, 420-433 (1996). DOI: 10.1006/cviu.1996.0069
30. Arcelli C, di Baja GS & Serino L. Distance-driven skeletonization in voxel images. *IEEE Trans Pattern Anal Mach Intell 33*, 709-720 (2011). DOI: 10.1109/TPAMI.2010.140
31. Palàgyi K & Kuba A. A 3D 6-subiteration thinning algorithm for extracting medial lines. *Patter Recognition Letters 19*, 613-627 (1998). DOI: 10.1016/S0167-8655(98)00031-2
32. Silvela J & Portillo J. Breadth-first search and its application to image processing problems. *IEEE Trans Image Process 10*, 1194-1199 (2001). DOI: 10.1109/83.935035
33. Kopechek JA, Haworth KJ, Raymond JL, Douglas Mast T, Perrin SR, Klegerman ME, Huang S, Porter TM, McPherson DD & Holland CK. Acoustic characterization of echogenic liposomes: frequency-dependent attenuation and backscatter. *The Journal of the Acoustical Society of America 130*, 3472-3481 (2011). DOI: 10.1121/1.3626124
34. Ishida O, Maruyama K, Sasaki K & Iwatsuru M. Size-dependent extravasation and interstitial localization of polyethyleneglycol liposomes in solid tumor-bearing mice. *Int J Pharm 190*, 49-56 (1999). DOI: 10.1016/S0378-5173(99)00256-2
35. Grouls C, Hatting M, Rix A, Pochon S, Lederle W, Tardy I, Kuhl CK, Trautwein C, Kiessling F & Palmowski M. Liver dysplasia: US molecular imaging with targeted contrast agent enables early assessment. *Radiology 267*, 487-495 (2013). DOI: 10.1148/radiol.13120220
36. Delli Castelli D, Dastru W, Terreno E, Cittadino E, Mainini F, Torres E, Spadaro M & Aime S. In vivo MRI multicontrast kinetic analysis of the uptake and intracellular trafficking of paramagnetically labeled liposomes. *J Control Release 144*, 271-279 (2010). DOI: 10.1016/j.jconrel.2010.03.005

Received: August 22, 2013; Revised: October 16, 2013; Accepted: October 24, 2013